Accepted Manuscript

Real time resistance monitoring during sintering of silver paste

Di Erick Xu, Jang Baeg Kim, Michael David Hook, Jae Pil Jung, Michael Mayer

PII: S0925-8388(17)33502-8

DOI: 10.1016/j.jallcom.2017.10.077

Reference: JALCOM 43474

To appear in: *Journal of Alloys and Compounds*

Received Date: 4 August 2017

Revised Date: 2 October 2017

Accepted Date: 10 October 2017

Please cite this article as: D.E. Xu, J.B. Kim, M.D. Hook, J.P. Jung, M. Mayer, Real time resistance monitoring during sintering of silver paste, *Journal of Alloys and Compounds* (2017), doi: 10.1016/j.jallcom.2017.10.077.

Real time resistance monitoring during sintering of silver paste

Di Erick Xu[1], Jang Baeg Kim[1,2], Michael David Hook[1], Jae Pil Jung[2], Michael Mayer[1]
1. Microjoining Laboratory, Centre for Advanced Materials Joining, Department of Mechanical and Mechatronics Engineering, University of Waterloo, Waterloo, Ontario, Canada N2L3G1
2. Microjoining and Semiconductor Packaging Lab, University of Seoul, Department of Materials Science and Engineering, 90 JunNong-dong, DongDaeMun-gu, Seoul 130-743, Korea

Abstract

Real time resistance monitoring technology is used to study the silver sintering process. Signals of joint resistance show events such as resistance increase to >10 GΩ, abrupt resistance drop from >10 GΩ to <1 kΩ, and gradual resistance drop to <1 mΩ. Based on cross-sectioning of samples at various stages of sintering and differential scanning calorimetry (DSC), we propose a correlation between resistance signal and solvent evaporation, capping agent degradation, and silver sintering. We identified distinct clusters of sintered silver of samples removed from the oven when the resistance drops to ~2.94 Ω.

Keywords: silver sintering paste, non-destructive signals, sintering process, real time monitoring

1. Introduction

Silver sintering pastes (SSPs) are used as die attachment material in microelectronics packaging, especially for power devices. [1] Some SSPs have lower bonding temperature than most solders, and can survive a higher temperature than some solder joints once bonded [1]. In some work [2-4], SSPs are added to epoxy based isotropically conductive adhesives (ICAs) to adjust the material property such as the conductivity.

Silver sintering pastes are typically mixtures of solvent, capping agent, and silver micro and/or nano particles. The silver particles are usually covered with a capping agent to avoid low temperature sintering. The silver sintering process is, for example in [5], a sequence of solvent evaporation, capping agent degradation, and silver sintering in elevated temperature according to the thermal gravimetric analysis (TGA). Generally, the smaller the particle sizes, the lower the sintering temperature needed [6]. Magdassi et al. have achieved room temperature sintering of 10 nm silver particles [7].

Despite the advantages of low process temperature, challenges remain for the current SSPs, such as the requirement for pressure to densify the joint, which increases the risk of cracking the brittle semiconductor, and thus can reduce the production yield [8]. To overcome such challenges, better SSP sintering process knowledge is required.

To improve the understanding of SSP sintering processes, a common way is to prepare samples at various sintering temperatures and times [5-7]. The samples are analyzed with microscopic images [5-7], thermal/electrical conductivity measurement [5], and shear/tensile test [6].

For example, Hu et al. [6] studied the tensile strength of silver sintering paste joint between copper wire to copper pad obtained at five temperatures between 100 °C and 300 °C. They found that the tensile strength increases with temperature for 250 µm wire, and remains unchanged

with 50 μm wire.

Alternatively, in-situ monitoring can provide real-time information for the sintering process, and transient phenomena can be studied with a fast enough sampling rate. A common in-situ monitoring technology to study SSP sintering process is TGA [1, 5, 9, 10].

For example, Lu et al. [5] used derivative thermogravimetric analysis to study six SSPs with different capping agents, and the same solvent α-Terpineol. For all the SSPs studied, the capping agent degradation happens after or in the end of solvent evaporation. Specifically, silver 2-ethylhexanoate decomposes at the lowest temperature of 190.3 °C. After 350 °C/30min processing, sintered silver is observed if the capping agent degradation temperature is lower than 250.2 °C.

Lately, resistance monitoring technology has been applied to study the curing process of epoxy-based ICA [11-14], while such study on SSP sintering process is not found. Inoue et al. [11, 13, 14] found that the change of electrical conductivity can not only be caused by curing reaction of the binder molecules, but also the conductivity change of the inter-filler chemicals, by comparing resistance signals with results from free-damped oscillation method.

Xiong et al. [12] obtained resistance-time curve with ICAs of 65 wt% silver fill loading. The resistance value becomes detectable (< 2.0 MΩ) at 27 min. In general, the resistance drops gradually, and it reaches 1.4 kΩ at 40 min, and 8.8 Ω at 80 min, respectively. After 80 min the resistance remains unchanged. The resistance decrement is explained with the epoxy resin shrinkage leading to an increase in the contact area between the fillers, which promote the formation of conductive pathways between the filler particles during the curing process.

In summary, in previous studies with resistance measurement for ICA curing process, the resistance values are measured at a few (<20) curing times and/or temperatures [5, 11, 12, 14-17],

and/or monitored with a slow sampling rate [12]. Some studies [3, 11-14] have missing resistance values because of the range limit of the technology applied. For example in [3], the maximum measurable resistance was 100 MΩ for the method used. When monitoring the ICA specimen resistance during curing, it exceeded the limit of 100 MΩ before the temperature reached 90 °C, and valid data was therefore not detected.

In this work, we study the sintering process of silver paste with an improved real time resistance monitoring technology based on the method used previously for a solder reflow study [18]. We present a larger range of resistance measurement (10^{-5}-10^{11} Ω), and provide a more continuous measurement than previous methods [3, 5, 10].

2. Experimental

2.1. Materials

The sample material is a commercially available SSP, Loctite Ablestik SSP 2020 [19-21]. The ingredients are shown in Table 1 [22]. The SSP is a silver sintering paste containing a mixture of silver particles, 2-(2-butoxyethoxy)ethyl acetate as capping agent, and 1,1'-oxydipropan-2-ol as solvent [23]. The optimal storage temperature is ≤40 °C [24].

2.2. Sample preparation

The SSP is dispensed with a Nordson Ultimus I automatic dispenser, with parameters shown in Table 2. The substrate is ceramic side-brazed dual in-line packages (Spectrum CSB02801). Figure 1 shows the top view optical image of the as dispensed samples. After dispensing, to minimize sample change such as room temperature sintering, or solvent vaporization, the sample is either used immediately, or covered and stored in a freezer at -40 °C. To minimize thawing issues such as the condensation of the moisture from air on the samples, the cover is always kept

on the substrate before the substrate reaches room temperature. The cover is ceramic, and a double sided Kapton tape is used to attach the cover to the substrate.

Figure 2 shows the sample design. Terminal numbers are indicated and the 12 resistance signals R1-R12 are defined.

2.3. Sintering and resistance measurements

The sintering profile recommended by the manufacturer is 4 hours at 175 °C. The oven is preheated to the sintering temperature. After the sample is connected, the resistance measurement starts running for 9 min in room temperature, with cover removed at 5 min, before the sample unit is placed into the oven. Four hours after placing the sample into the oven, the oven stops heating, and the samples are left inside the oven to cool down.

For the test setup, the oven, multiplexer, connecting materials, and temperature measurement are the same as in [18]. In addition, an Agilent B2911A precision source/measure unit and an Agilent 34420A nanovoltmeter is used for resistance measurement, in 2-wire mode (for >1 Ω) and 4-wire mode (for < 1Ω), respectively. The measuring process is controlled with a custom designed Matlab program [25]. The flow chart of an example monitoring process using this program is shown in Fig. 3. In this example, all 12 samples are monitored, and all resistance measurement modes are enabled. Alternatively, the monitoring process can be done on fewer samples, and/or with fewer resistance measurement modes, for faster sampling rate.

Figures 4a and b show the connection schemes used for resistance measuring with 2-wire and 4-wire, respectively. Samples R1-R12 are connected to and measured by the test equipment sequentially, by closing one of the 12 switches while opening the other 11 switches in each measurement loop. Both *R-t* and *T-t* curves are visualized in real time on the PC screen.

2.4. Cross sectioning of interrupted samples

Some samples are interrupted at various times when special events on the resistance signal appear during the sintering process, and are taken out of the oven to cool in air for subsequent cross sectional studies.

The final polishing is done manually with 0.1 µm diamond paste for sufficiently hard samples, and no smearing issue is encountered. Some not fully sintered samples are too soft to be polished mechanically at room temperature, and thus are cooled down to -40 °C with liquid nitrogen, and ion milled. No cracks are observed for the samples milled at -40 °C.

3. Results

3.1. Sample images and geometry

Figures 5a-b show the top view microscopic images of the SSP sample before, and after sintering, all taken with environmental scanning electron microscope (ESEM, WATlab at University of Waterloo). The particles are characterized with the intercept method, and the average linear intercepts are 1.79, and 1.86 µm for Figs. 5a, and b, respectively.

Figure 6a shows example cross-sectional outlines of the sample before and after sintering at the same sectioning location. The coordinates of the points are measured with an optical microscope from the top, and an example image is shown in Fig. 6b. In Fig. 6a, the lines are obtained with piecewise cubic interpolation. The areas are calculated with trapezoidal numerical integration. The numbers are from four pairs of samples. The amount of SSP between lead finger centers is estimated to be 0.78 ± 0.07 mg before curing.

3.2. Resistance signals

Figure 7 shows the overview of an example result from the SSP sintering. Figures 8-9 show

zoomed in parts from typical *R-t* and *T-t* curves. On the *R-t* curves of Figs. 8a and c, we make a sequence of six observations: 1. room temperature high resistance of 10^6-10^9 Ω, 2. resistance drop and rise forming a "V" shape signal until >10 GΩ, and 3. stable high resistance of 10-30 GΩ, 4. abrupt resistance drop from >10 GΩ to <1 kΩ, 5. steady resistance drop down to <1 mΩ, and 6. resistance change mainly following the temperature change.

A set of characteristic quantities is derived from the *R-t* curve, as shown in Figs. 8a-c, and the values are shown in Table 3. R_0 and R_f are initial and final resistances at room temperature, which is approximately 25 °C, t_1 is the time after when the resistance signal is >10 GΩ, and T_1 is the corresponding temperature, t_2 is the time after when the resistance signal is <1 kΩ, and T_2 is the corresponding temperature, t_3 is the time when the resistance signal is 5 Ω, and T_3 is the corresponding temperature. The different sample size in Table 3 is because of the use of some incomplete *R-t* profiles. During the development of the technology, we often obtain incomplete *R-t* profiles due to the large range of *R* change in sintering, and the limited range of test equipment in use.

Figure 10 shows a typical *R-T* curve during cooling. The *R-T* relation is linear. *R* values are interpolated at temperatures *T* = 60, 70,..., 170 °C and plot vs. *T* to determine the d*R*/d*T* slopes, resulting in correlation coefficient of >0.99 and slopes average and standard error of 2.60, and 0.06 μΩ/°C, respectively (182 samples). The temperature coefficient of resistance (TCR) is α = 4.31 ± 0.02 [10^{-3}K^{-1}], while the TCR of silver [26] is α_{Ag} = 3.8 [10^{-3}K^{-1}]. R_{ref} is the extrapolated resistance value at T_{ref}, and T_{ref} is the reference temperature 20 °C in this work.

3.3. Determining the resistivity of sintered paste

Figure 11 shows the geometry of a finite element (FE) model for a sintered sample segment, where the cross section of the sintered paste is taken from Fig. 6. The conductivity of the lead

fingers is that of Ni 14.3 MS/m. The resistance calculation method is shown in Fig. 12.

Figure 13 shows the dependence of R_{fem} from the FE study on the SSP conductivity (σ_{SSP}). Taking the value of R_f shown in Table 3, the resistivity of the sintered SSP is thus calculated as 55-180 nΩ•m, while the resistivity of pure Ag is 1.59 nΩ•m [26].

3.4. Microscopy of interrupted samples

Figures 14a-d show the cross sectional images of the interrupted samples. Specifically, we took samples out of the oven around t_1, t_2 and t_3, respectively. After reviewing the *R-t* signals, we learn that the sample in Fig. 14a is taken out of the oven at about t_1 + 5.4 min, and the resistance signal stays >10 GΩ afterwards. The sample in Fig. 14b is taken out of the oven at about t_2 + 2.5 min and the final resistance is 253.2 Ω with standard deviation of 233.5 Ω, ranging from 27.22 Ω to 803.7 Ω. The large resistance range possibly results from the fast transition of resistance value at about t_2 + 2.5 min. The sample in Fig. 14c is taken out of the oven at about t_3 and its resistance is 2.94 Ω measured at room temperature. In Fig. 14d, the sample sintering is finished (t = 600 min). The particles in Figs. 14a, b, and d are characterized with the intercept method, and the average linear intercepts are 0.77, 0.63, and 1.19 µm, respectively.

As the solvent evaporation continues during cross-section sample preparation, we assume negligible amount of remaining solvent exists in any of the samples shown in Figs. 14a-d.

Figures 14a and b show high similarity, where we can mainly see a crowd of 200 nm - 4 µm silver particles. Figure 14c shows a cluster of sintered silver particles in the center as indicated with the arrow, and is otherwise the same as Figs. 14a and b. Three instances of sintered silver clusters made from particles smaller than 1 µm are found in a 500 µm × 200 µm cross-section segment. The distance between neighboring clusters found is >50 µm. Figure 14d shows a connected network of sintered silver obtained after 600 min. The sintered network appears

denser in a cross-sectional image (Fig. 14d) than a top view image (Fig. 5b), where joints tend to be covered by the particles.

3.5. Open pan DSC

Figures 15a and b show the ramping and isothermal segments of an open pan DSC study of the SSP, respectively. There was no air flow in the experiment. The temperature profile is set to ramp at 10 °C/min from room temperature to 175 °C, and hold at 175 °C for 10 h. The data after 350 min at 175 °C has no obvious peaks, and is not shown. The noise due to temperature profile change is shown in light green color.

One endothermic peak of -33.7 mW/g is observed during ramping stage at 147.7 °C, which is possibly caused by solvent evaporation. The endothermic heat flow for solvent evaporation typically increases with temperature, and decreases as the remaining solvent becomes less, resulting in an endothermic peak. Two exothermic peaks of 9.9, and 20.2 mW/g are observed during isothermal stage after 26.3 min and 107.8 min at 175 °C, respectively, which are possibly caused by capping agent degradation, and silver sintering, respectively. The capping agent degradation may involve oxidation or even combustion [27-29].

The sample mass before and after the DSC test are 20.8 and 18.8 mg, respectively, as measured using a Sartorius CP124S analytical balance, which has a resolution of 0.1 mg, and a range of 120 g. The mass loss is 9.6 %.

4. Discussion

This section discusses the observations and gives possible explanations. Figure 16 shows a proposed correlation between the resistance signal and the sintering process.

4.1. Solvent evaporation and capping degradation

Initially, due to the existence of solvent and capping agent, it is difficult for free electrons to move between silver particles, leading to high value of R_0. The resistance is dominated by ions in the solvent. Both organic chemicals shown in Table 1 are polar molecules, and dissolve free ions, including Cl^-, K^+, and Na^+ [24].

The main event in the early stage of the sintering process is solvent evaporation [30]. According to the DSC study shown in Fig. 15a, the solvent evaporation peak temperature is 147.7 °C. During solvent evaporation we observe resistance decrement and a subsequent resistance increment from the *R-t* curve as shown in Fig. 8a. The resistance decrement is due to the temperature rise as ion mobility increases with temperature [31]. The subsequent resistance increment is caused by the solution amount decrement due to solvent evaporation. At and above T_1, the solvent has evaporated, leading to the ion becoming immobile, which is equivalent to losing the electrical conduction property, causing the resistance to increase strongly.

Between t_1 and t_2, the remaining conducting ions are too few to contribute to the sample conductivity. The high resistance values of 10-30 GΩ are dominated by the insulating property of the capping agent [7].

The capping agent degradation mainly starts after solvent evaporation [32, 33], which is around t_1. The capping agent degradation gradually makes the formation of conductive path easier [7]. The resistance drop at t_2 is possibly caused by the formation of the first conductive path. The steady resistance drop between t_2 and t_3 is possibly caused by further degradation of the capping agent and the formation of more conductive paths.

According to the DSC study shown in Fig. 15b, the capping agent degradation peak time is 26.3 min at 175 °C, which approximates t_3 (27.1 min in oven). The heat generated from capping

degradation may add to the triggering of Ag sintering at t_3.

4.2. Silver sintering

The Ag sintering starts between t_2 and t_3, according to the observation of the first sintered Ag particle clusters observed in Fig. 14c. Without capping agent, bare Ag particles are readily joined together [33]. The driving force $\Delta\mu$ is the chemical potential difference between the atoms on the surface and in the bulk, given by [34]:

where $\Omega=1.7\times10^{-29}$ m^3 is the volume per atom in the solid silver bulk according to its lattice structure; γ is the surface tension, theoretically 890 mJ/m^2 [35] and independent of particle size for down to 4-atom clusters [36-38] for solid silver; and R_1 and R_2 are the principal radii of curvature of the surface. For a spherical particle, $1/R_1+1/R_2$ and thus $\Delta\mu$ are the same along the surface. For a flake, $1/R_1+1/R_2$ and thus $\Delta\mu$ are largest on the edge. The thinner the flake, the higher $\Delta\mu$.

The $\Delta\mu$ drives surface atoms to diffuse to the bulk, or a surface with lower value of $1/R_1+1/R_2$. In a mixture of Ag particles, such diffusion can result in particle joining or particle shape change [33], typically reducing the total surface area.

In the case of particle joining, the atoms on the joining surfaces become bulk atoms, and thus the $\Delta\mu$ is reduced for these atoms. Since the joining surfaces become bulk on both sides, the total surface area is reduced by approximately twice the joining area. In the case of particle shape change, a flake may change into a few small spheres. For example, for a 4 µm diameter and 100 nm thick round-edged disc (see label E in Fig. 14b), the $\Delta\mu$ is 3.1×10^{-22} J on the edge, the volume is 1.3 µm^3, and the total surface area is 27.1 µm^2, assuming the round-edge radius is half of the disc thickness. If it breaks into four identical spheres, assuming no total volume change, the $\Delta\mu$ is 7.1×10^{-23} J on the surface, the radius is 0.43 µm, and the total surface area is 9.1 µm^2.

As a result, the maximum atomic $\Delta\mu$ is reduced by 77.1 %, and the total surface area is reduced by 66.4 %.

After t_3, the resistance drop is mainly caused by further Ag sintering and particle size growth in the sintered percolation network. Growth of sintered particles is observed in this work from comparing the cluster in Fig. 14c and the network in Fig. 14d. A larger size particle typically has lower average atomic $\Delta\mu$ because of the smaller surface area to volume ratio and a smaller $1/R_1+1/R_2$ value on the surface. For example, if four radius 0.43 µm spheres merge to form one large sphere without volume change, the total surface area change from 9.1 μm^2 to 5.8 μm^2, reducing by 36 %, and the surface $\Delta\mu$ changes from 7.1×10^{-23} J to 4.5×10^{-23} J, reducing by 37 %. Assuming the number of surface atoms is proportional to the surface area, the average $\Delta\mu$ is thus reduced by 60 %.

5. Conclusions

Real time resistance monitoring technology is developed to study the process of silver sintering. The characteristic *R-t* relationship is obtained for the example SSP studied. The resistance change is explained with the physical and metallurgical evolution of the SSP during the sintering process, with the help of DSC and existing knowledge for SSP sintering. Essential mechanisms are detected with resistance signals, including solvent evaporation, capping agent degradation, and formation of first sintered clusters.

The resistance monitoring technology could be tested for process control with a real time feedback loop during the sintering process, and also for gaining knowledge and development of new SSP materials. For example, the resistance monitoring technology can help optimize the composition including the solvent, capping agent, nano-particles and micro-particles, and the sintering parameters, to achieve minimized final resistance. Moreover, *R-t* signals for nano

particle Ag paste sintering process can be studied and compared with the mixed paste sintering process, which is composed of Ag nano and micro particles. Ultimately, the resistance monitoring technology may help overcome some current and/or future challenges in electronics packaging industry, such as increasing power density.

Acknowledgments

This work is supported by the Natural Science and Engineering Research Council (NSERC), and Microbonds Inc., Markham (both from Canada). The authors are grateful for Geoff Rivers, who helped with DSC experiments. We thank for the free sample from Henkel Inc.

References

[1] Wang T, Chen X, Lu GQ, Lei GY. Low-temperature sintering with nano-silver paste in die-attached interconnection. journal of electronic materials. 2007 Oct 1;36(10):1333-40.

[2] Zhang R, Moon KS, Lin W, Wong CP. Preparation of highly conductive polymer nanocomposites by low temperature sintering of silver nanoparticles. Journal of Materials Chemistry. 2010;20(10):2018-23.

[3] Rivers G, Marzbanrad E, Hook MD, Lee-Sullivan P, Zhou YN, Zhao B. Highly-stable silver nanobelts joined via diffusion-free attachment. Nanotechnology. 2016 Jun 13;27(29):295606.

[4] Pashayi K, Fard HR, Lai F, Iruvanti S, Plawsky J, Borca-Tasciuc T. High thermal conductivity epoxy-silver composites based on self-constructed nanostructured metallic networks. Journal of Applied Physics. 2012 May 15;111(10):104310.

[5] Lu CA, Lin P, Lin HC, Wang SF. Effects of metallo-organic decomposition agents on thermal decomposition and electrical conductivity of low-temperature-curing silver paste. Japanese journal of applied physics. 2006 Sep 7;45(9R):6987.

[6] Hu A, Guo JY, Alarifi H, Patane G, Zhou Y, Compagnini G, Xu CX. Low temperature sintering of Ag nanoparticles for flexible electronics packaging. Applied Physics Letters. 2010 Oct 11;97(15):153117.

[7] Magdassi S, Grouchko M, Berezin O, Kamyshny A. Triggering the sintering of silver nanoparticles at room temperature. ACS nano. 2010 Apr 7;4(4):1943-8.

[8] Siow KS. Are sintered silver joints ready for use as interconnect material in microelectronic packaging?. Journal of electronic materials. 2014 Apr 1;43(4):947.

[9] Zhang Z, Lu GQ. Pressure-assisted low-temperature sintering of silver paste as an alternative die-attach solution to solder reflow. IEEE Transactions on electronics packaging manufacturing. 2002 Oct;25(4):279-83.

[10] Lei TG, Calata JN, Lu GQ, Chen X, Luo S. Low-Temperature Sintering of Nanoscale Silver Paste for Attaching Large-Area (>100 mm^2) Chips. IEEE Transactions on Components and Packaging Technologies. 2010 Mar;33(1):98-104.

[11] Sakaniwa Y, Iida M, Tada Y, Inoue M. Conduction path development in electrically conductive adhesives composed of an epoxy-based binder. Electronics Packaging and iMAPS All Asia Conference (ICEP-IACC), 2015 International Conference on 2015 Apr 14 (pp. 252-257). IEEE.

[12] Xiong N, Li Z, Li J, Xie H, Wang Y. Influence of curing procedures on the electrical properties of epoxy-based isotropic conductive adhesives. In Proc. Electronic Packaging Technology (ICEPT), 2014 15th International Conference on 2014 Aug 12 (pp. 373-377). IEEE.

[13] Inoue M, Sakaniwa Y, Tada Y. In-situ analysis of electrical conductivity evolution in epoxy-based conductive adhesives with Ag loading during curing process. CPMT Symposium Japan (ICSJ), 2014 IEEE 2014 Nov 4 (pp. 190-193). IEEE.

[14] Sakaniwa Y, Tada Y, Inoue M. Effect of chemical factors on the evolution of electrical conductivity during curing in Ag-loaded conductive adhesives composed of an epoxy-based binder—A new understanding of electrically conductive adhesives. Electronics Packaging (ICEP), 2014 International Conference on 2014 Apr 23 (pp. 176-180). IEEE.

[15] Cui HW, Fan Q, Li DS, Tang X. Formulation and characterization of electrically conductive adhesives for electronic packaging. The Journal of Adhesion. 2013 Jan 1;89(1):19-36.

[16] Cui HW, Jiu JT, Nagao S, Sugahara T, Suganuma K, Uchida H, Schroder KA. Ultra-fast photonic curing of electrically conductive adhesives fabricated from vinyl ester resin and silver micro-flakes for printed electronics. RSC Advances. 2014;4(31):15914-22.

[17] Cui HW, Du WH. Novel Fast-Curing Electrically Conductive Adhesives from a Functional Epoxy and Micro Silver Flakes: Preparation, Characterization, and Humid-Thermal Aging. The Journal of Adhesion. 2013 Sep 2;89(9):714-26.

[18] Xu DE, Hook MD, Mayer M. Real time joint resistance monitoring during solder reflow. Journal of Alloys and Compounds. 2016 Nov 25.

[19] Yu F, Cui J, Zhou Z, Fang K, Johnson RW, Hamilton MC. Reliability of Ag Sintering for Power Semiconductor Die Attach in High Temperature Applications. IEEE Transactions on Power Electronics. 2016 Nov 21.

[20] Modugno MC, Wereszczak AA, Waters SB. Toward Interpreting Failure in Sintered-Silver Interconnection Systems. Additional Papers and Presentations. 2016 Jan;2016(HiTEC):000234-41.

[21] Wereszczak AA, Modugno MC, Waters SB, DeVoto DJ, Paret PP. Method to Determine Maximum Allowable Sinterable Silver Interconnect Size. Additional Papers and Presentations. 2016 Jan;2016(HiTsEC):000207-15.

[22] LOCTITE ABLESTIK SSP 2020 MSDS [Online]; Henkel Electronic Materials LLC: Irvine, CA, Oct 23, 2014. http://hybris.cms.henkel.com/henkel/msdspdf?matnr=1735608&country=US&language=EN (accessed Feb 27, 2017).

[23] Jenny England, Xinpei Cao, Hajime Inoue, Steven Josso, Anja Henckens. Silver Sintering for Power Electronics. MEPTEC, October 23, 2014

[24] LOCTITE ABLESTIK SSP 2020 Technical Data Sheet [Online]; Henkel Electronic Materials LLC: Irvine, CA, Oct, 2012. https://tds.us.henkel.com/NA/UT/HNAUTTDS.nsf/web/07277E203E5FED5E85257B080060D5FE/$File/LOCTITE%20ABLESTIK%20SSP%202020-EN.pdf (accessed Mar 07, 2017).

[25] Matlab code filename RmonitoringSSP_v20170802.m (https://www.mathworks.com/matlabcentral/fileexchange/63963-resistance-monitoring-of-silver-sintering-process or http://www.eng.uwaterloo.ca/~d9xu/)

[26] Kuphaldt TR. Lessons from electric circuits, Volume I – DC, Chapter 12 - Physics Of Conductors And Insulators. (2007)

[27] Lu D, Tong QK, Wong CP. A study of lubricants on silver flakes for microelectronics conductive adhesives. IEEE Transactions on Components and Packaging Technologies. 1999 Sep;22(3):365-71.

[28] Lu D, Wong C. Thermal decomposition of silver flake lubricants. Journal of thermal analysis and calorimetry. 2000 Jul 1;61(1):3-12.

[29] Akada Y, Tatsumi H, Yamaguchi T, Hirose A, Morita T, Ide E. Interfacial bonding mechanism using silver metallo-organic nanoparticles to bulk metals and observation of sintering behavior. Materials transactions. 2008 Jul 1;49(7):1537-45.

[30] Wakuda D, Kim KS, Suganuma K. Room temperature sintering of Ag nanoparticles by drying solvent. Scripta Materialia. 2008 Sep 30;59(6):649-52.

[31] Biswas R, Bagchi B. Limiting ionic conductance of symmetrical, rigid ions in aqueous solutions: temperature dependence and solvent isotope effects. Journal of the American Chemical Society. 1997 Jun 25;119(25):5946-53.

[32] Ide E, Angata S, Hirose A, Kobayashi KF. Metal–metal bonding process using Ag metallo-organic nanoparticles. Acta materialia. 2005 May 31;53(8):2385-93.

[33] Peng P, Hu A, Gerlich AP, Liu Y, Zhou YN. Self-generated local heating induced nanojoining for room temperature pressureless flexible electronic packaging. Scientific reports. 2015;5.

[34] Zhou W, Zheng Z, Wang C, Wang Z, An R. One-Step Fabrication of 3D Nanohierarchical Nickel Nanomace Array To Sinter with Silver NPs and the Interfacial Analysis. ACS applied materials & interfaces. 2017 Jan 30;9(5):4798-807.

[35] Kinloch A. Adhesion and adhesives: science and technology. Springer Science & Business Media; 2012 Dec 6.

[36] Lewis B. The enhanced vapour pressure of small clusters. Thin Solid Films. 1972 Feb 1;9(2):305-8.

[37] Chernov SF, Fedorov YV, Zakharov VN. Surface tension of silver in different media. Journal of Physics and Chemistry of Solids. 1993 Aug 1;54(8):963-6.

[38] Lu HM, Jiang Q. Size-dependent surface tension and Tolman's length of droplets. Langmuir. 2005 Jan 18;21(2):779-81.

Table 1. SSP ingredients [22]

Chemical name	wt.%
silver flakes and spheres	balance
2-(2-butoxyethoxy)ethyl acetate (capping agent, boiling point 245 °C, flash point 102 °C)	1-5
1,1'-oxydipropan-2-ol (solvent, boiling point 232.8 °C, flash point 138 °C)	1-5

Table 2. Dispensing parameters

Tip inner diameter [mm]	Speed [mm/s]	Pressure [psi]
0.33	4	15

Table 3. Characteristic values in sintering (average and standard deviation)

	μ	σ	sample size
log (R_0/1Ω)	7.3	0.5	222
t_1 [min]	15.1	0.6	63
T_1 [°C]	133.8	5.5	63
t_2 [min]	30.4	3.5	83
T_2 [°C]	168.8	1.2	83
t_3 [min]	36.1	5.6	214
T_3 [°C]	170.7	1.2	214
R_f [mΩ]	0.54	0.25	148

- Silver sintering process is studied with **real time resistance monitoring** method.
- A **large range** between >10GΩ and < 1mΩ in the sintering process is recorded.
- **Special events** on *R-t* signals are identified, including solvent vaporization.
- **Nano-link cluster formation** is observed for the first time in cross sections.

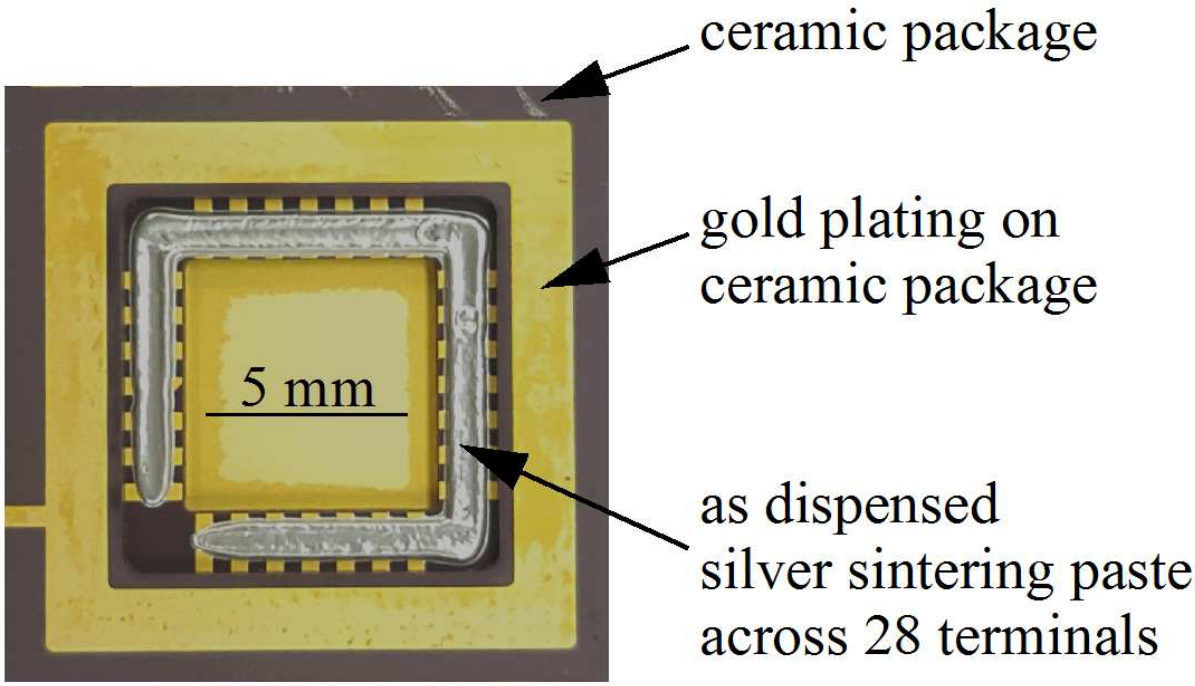

Figure 1. A top view optical image of the ceramic package with the as dispensed SSP.

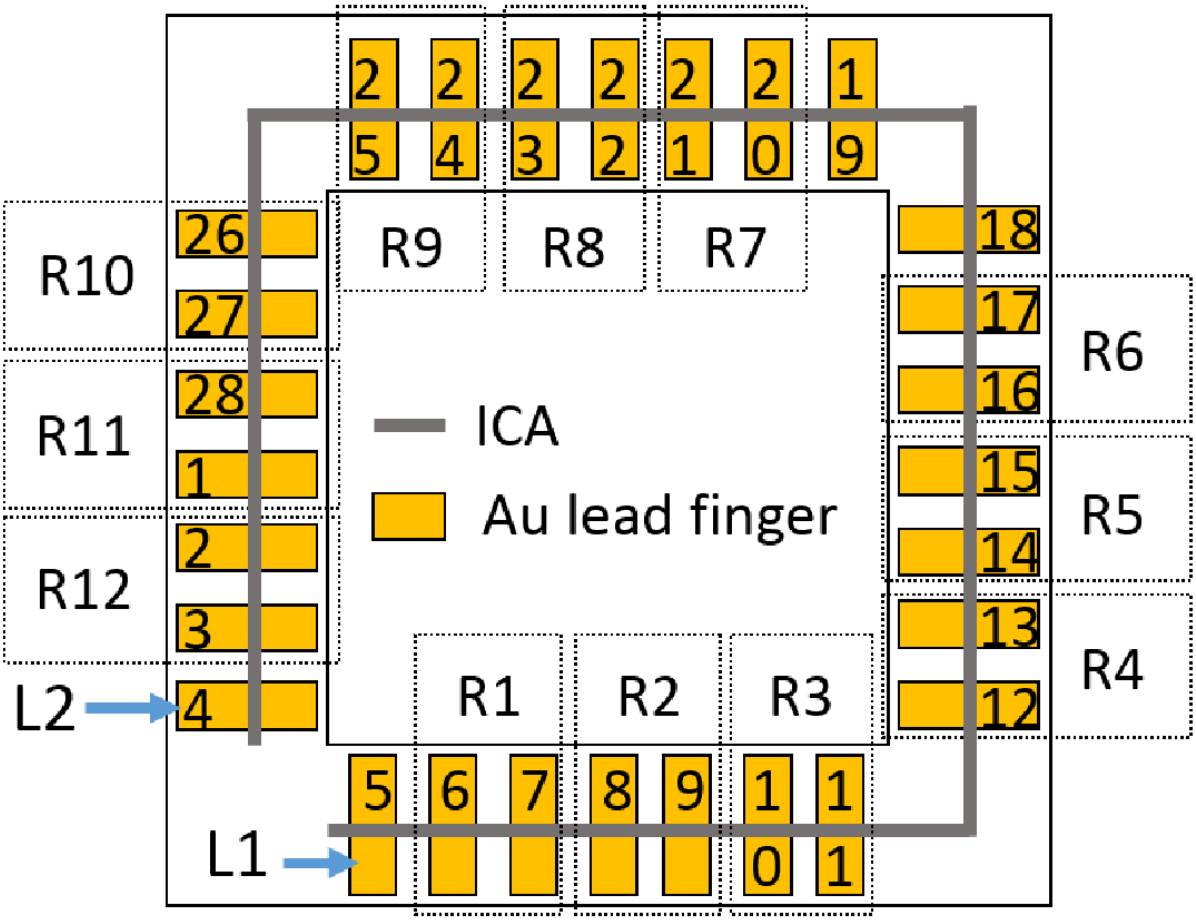

Figure 2. SSP resistance measurement scheme.

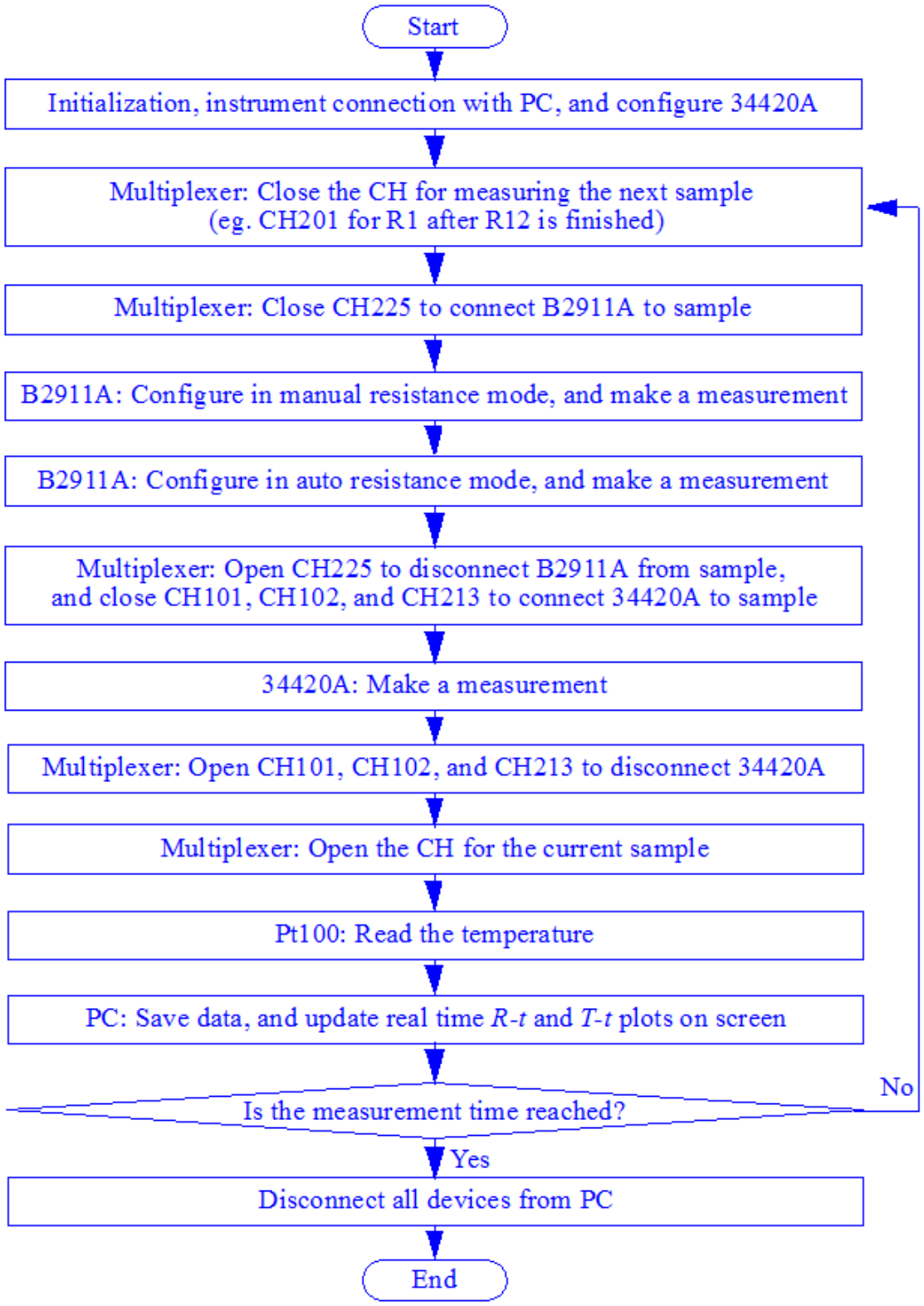

Figure 3. Matlab program flow chart of an example monitoring process during silver sintering [25].

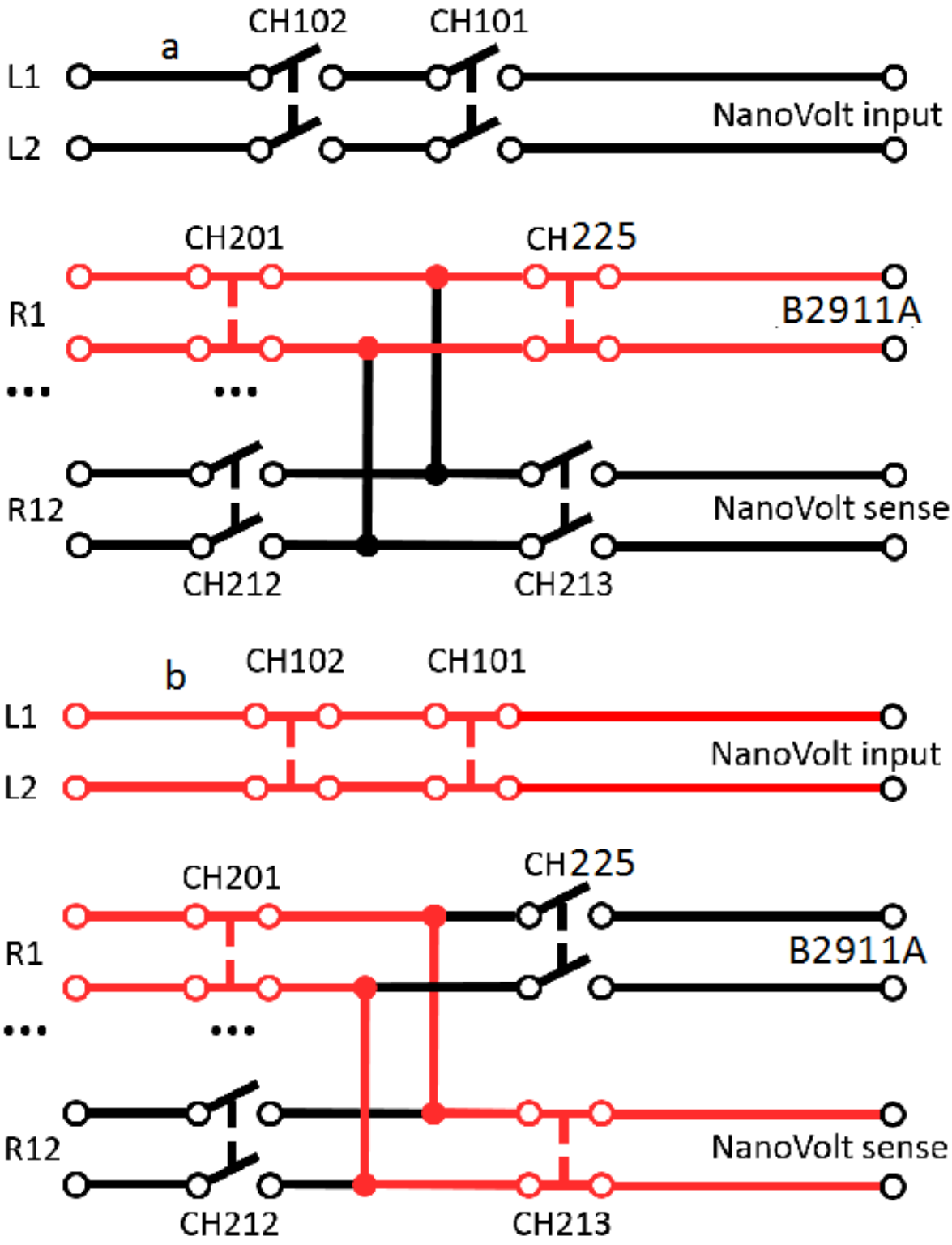

Figure 4. Connection scheme for resistance measurement in (a) 2-wire, and (b) 4-wire modes, respectively. CH numbers identify switches within the equipment.

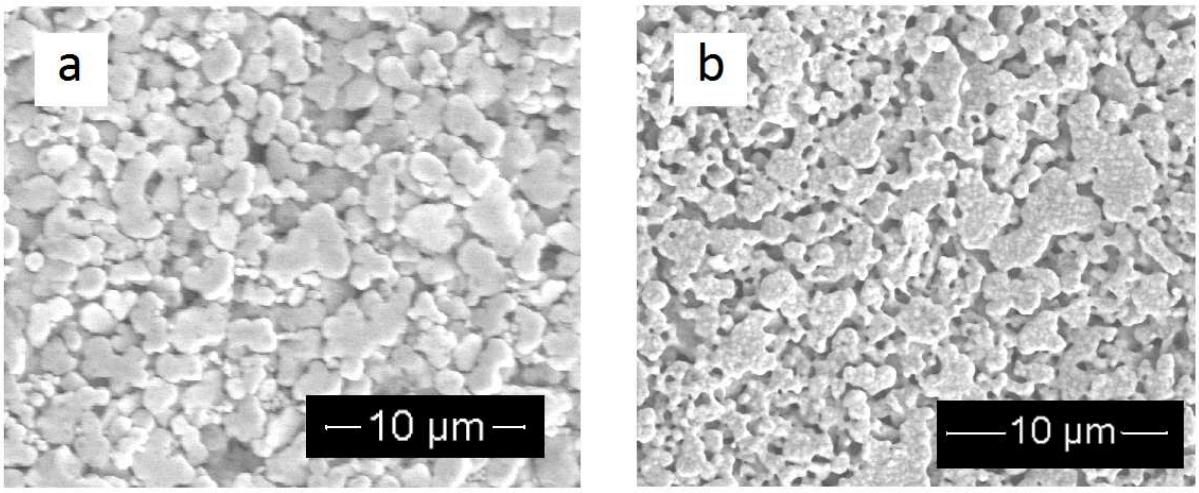

Figure 5. Top view microscopic images of (a) as dispensed SSP, (b) sintered SSP, both taken with environmental scanning electron microscope (ESEM, Watlab at University of Waterloo).

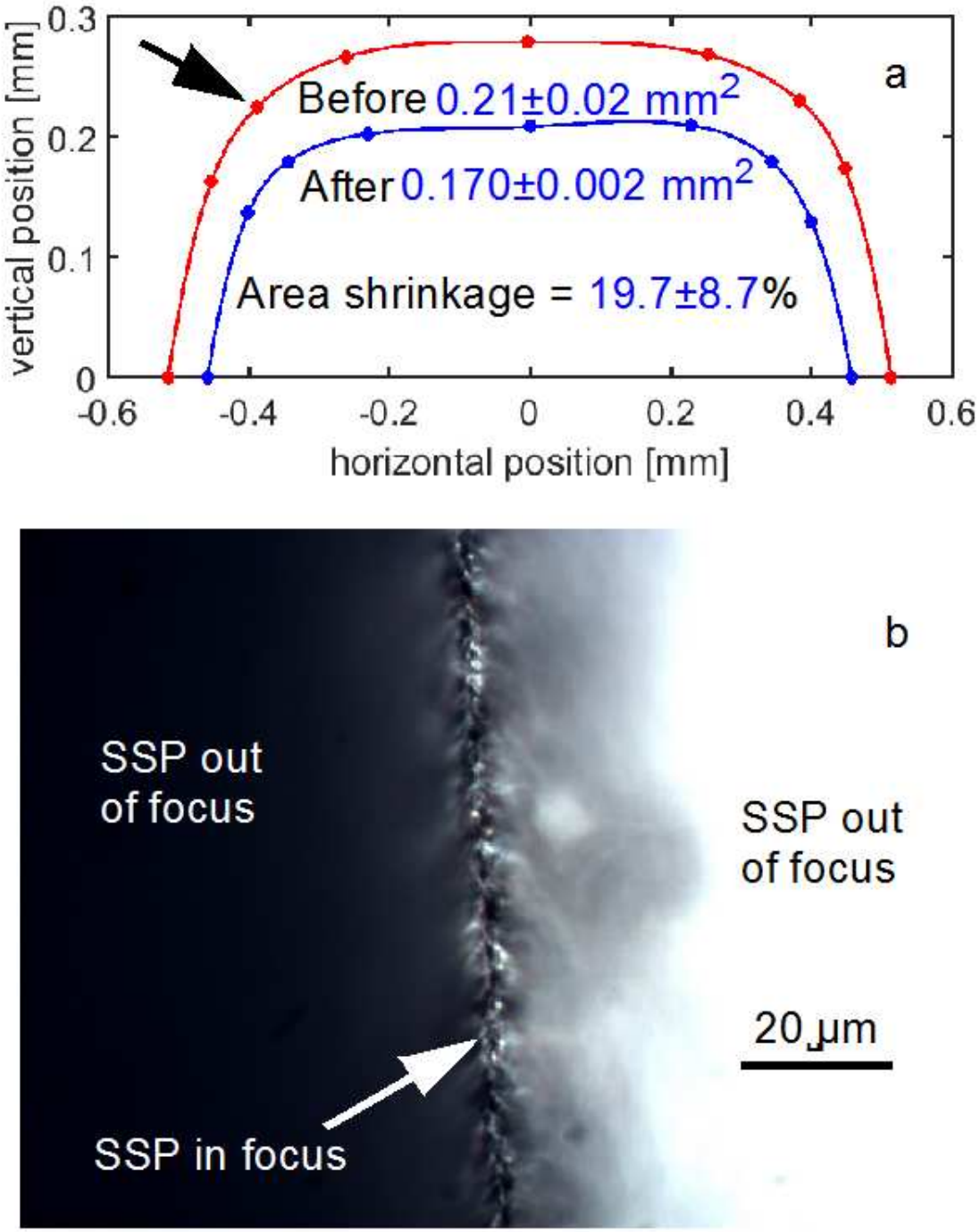

Figure 6. (a) Cross-sectional outlines of the SSP before and after sintering, measured with optical microscope at the same sectioning location on the sample. Cross-sectional areas are calculated with piecewise cubic interpolation and trapezoidal numerical integration. (b) Top view image for measuring the coordinate of the point indicated in (a) with the arrow.

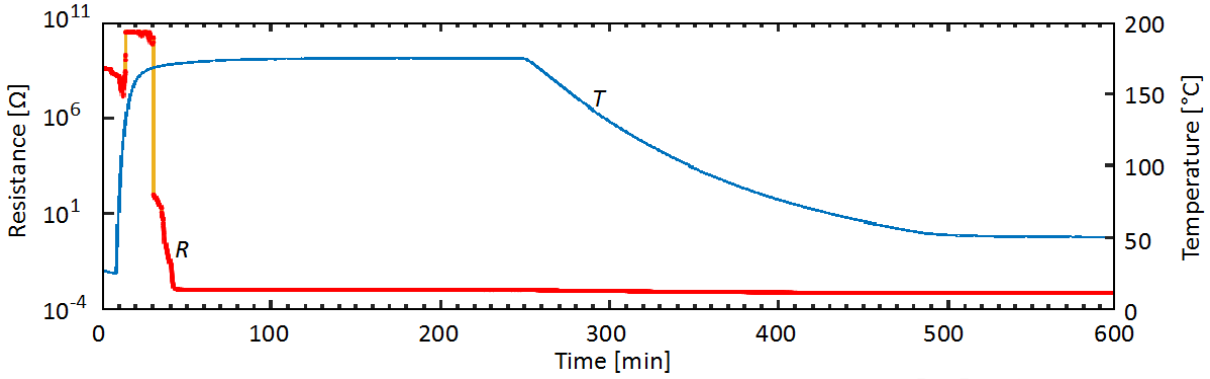

Figure 7. Typical *R*-*t* and *T*-*t* curves during the SSP sintering.

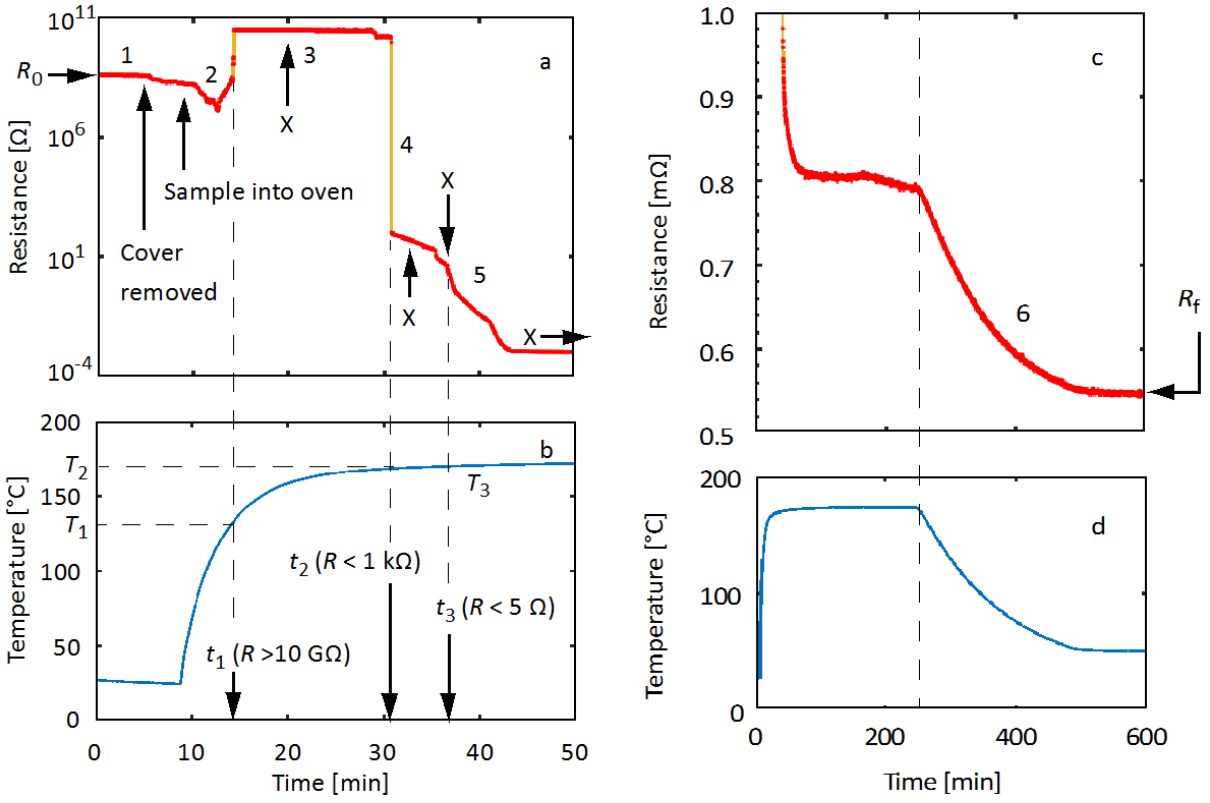

Figure 8. (a) *R*-*t* curve zoomed at 0-50 min, label X's indicates times when cross-sections are taken. (b) corresponding *T*-*t* curve, (c) *R*-*t* curve zoomed to 0.5-1 mΩ, and (d) corresponding *T*-*t* curve.

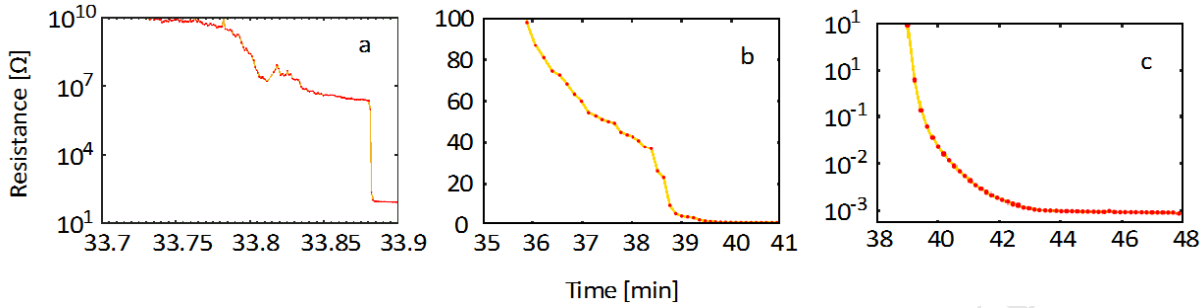

Figure 9. Example *R-t* curves zoomed at (a) around t_2 (33.7-33.9 min), (b) around t_3 (0-100 Ω, 35-41 min), and (c) after t_3 (0.5 mΩ-10 Ω, 38-48 min), respectively.

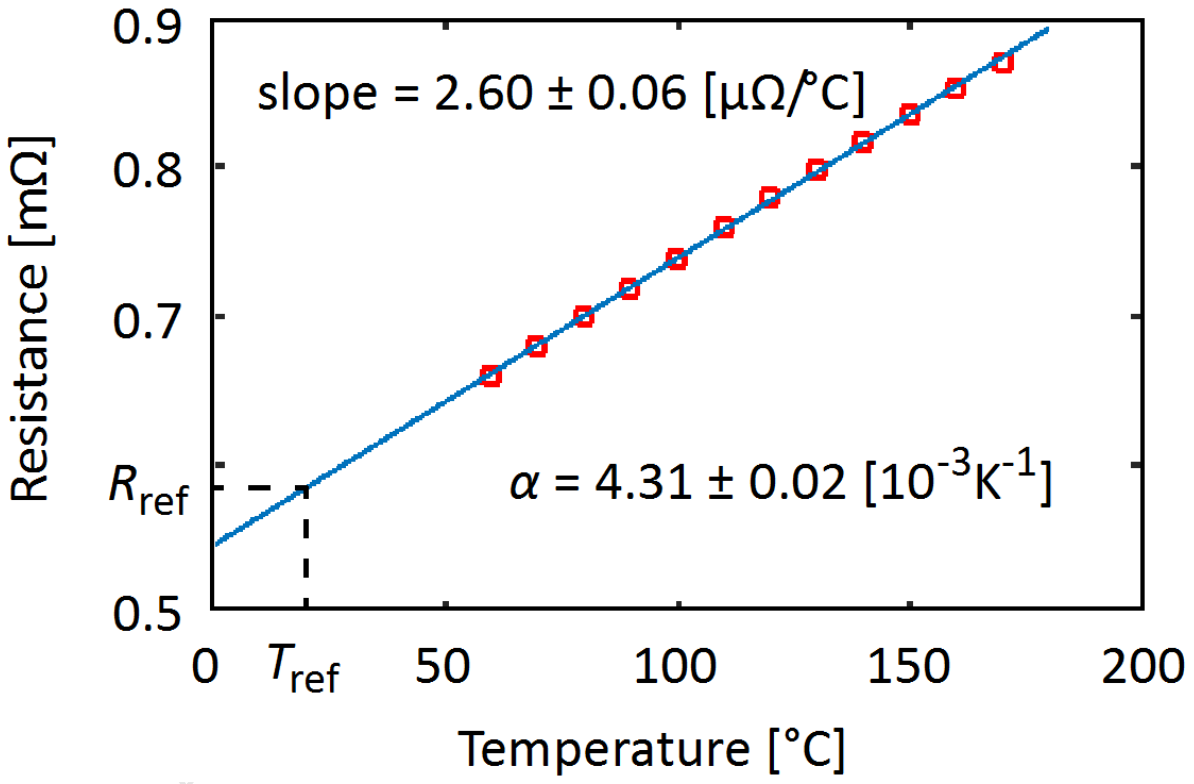

Figure 10. An example *R-T* curve in cooling stage of the sintering process. The TCR value is calculated with a reference temperature of 20 °C. The values shown are average ± standard error, with 182 samples.

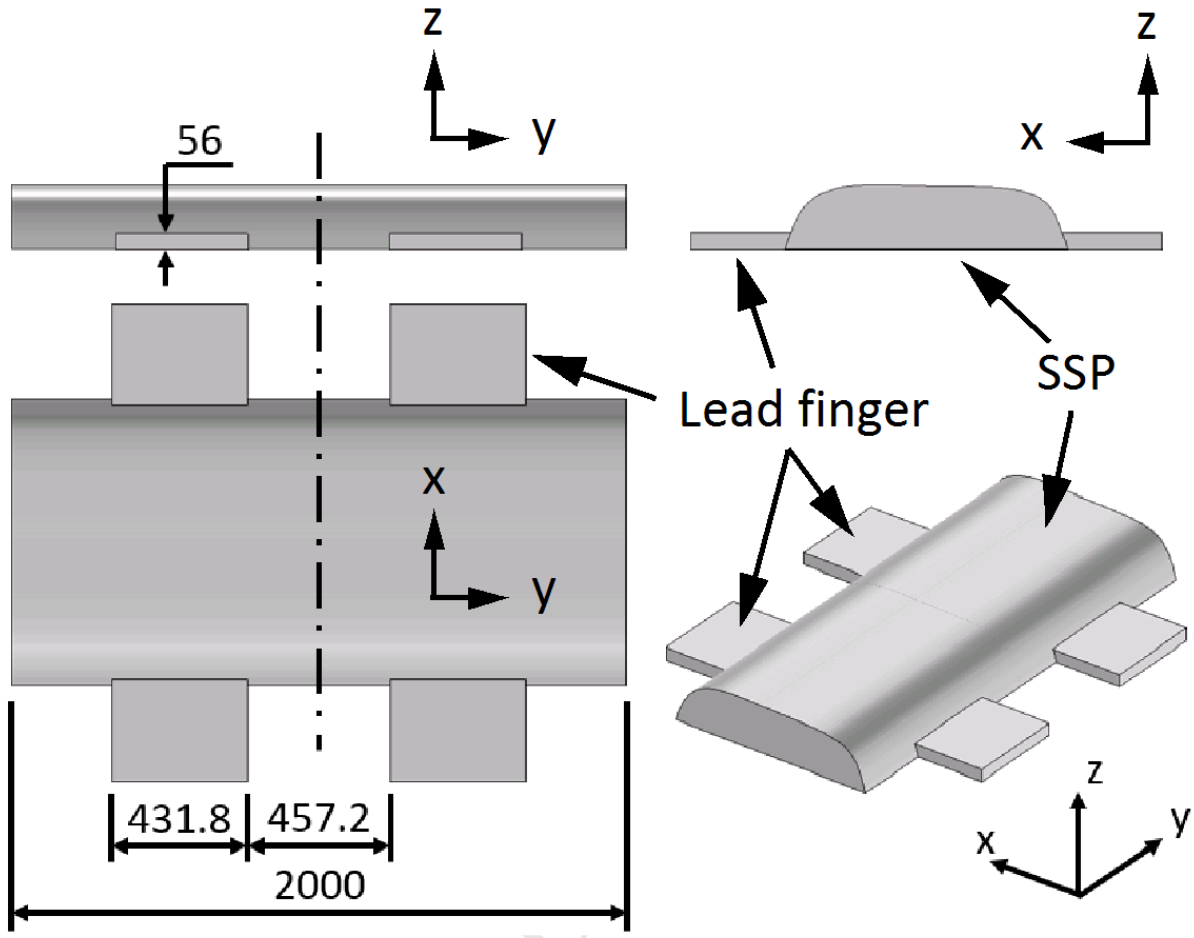

Figure 11. FE model geometry (unit: μm), outline of SSP after sintering taken from Fig. 5.

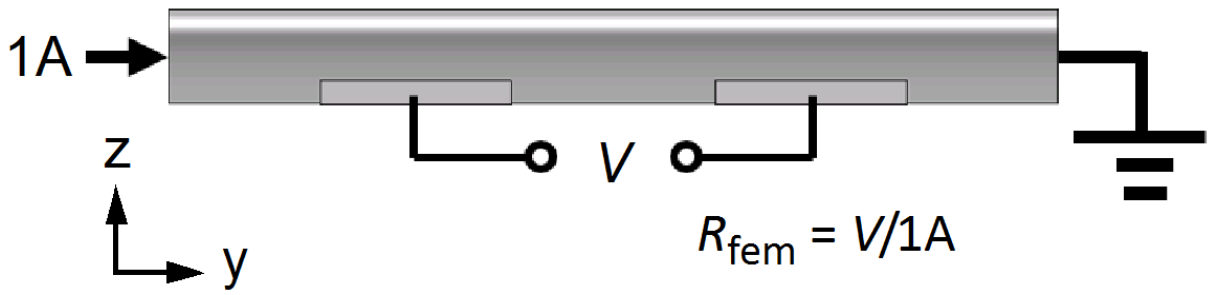

Figure 12. Resistance calculation with FE model (side view), where V is the difference between the two surface average potentials.

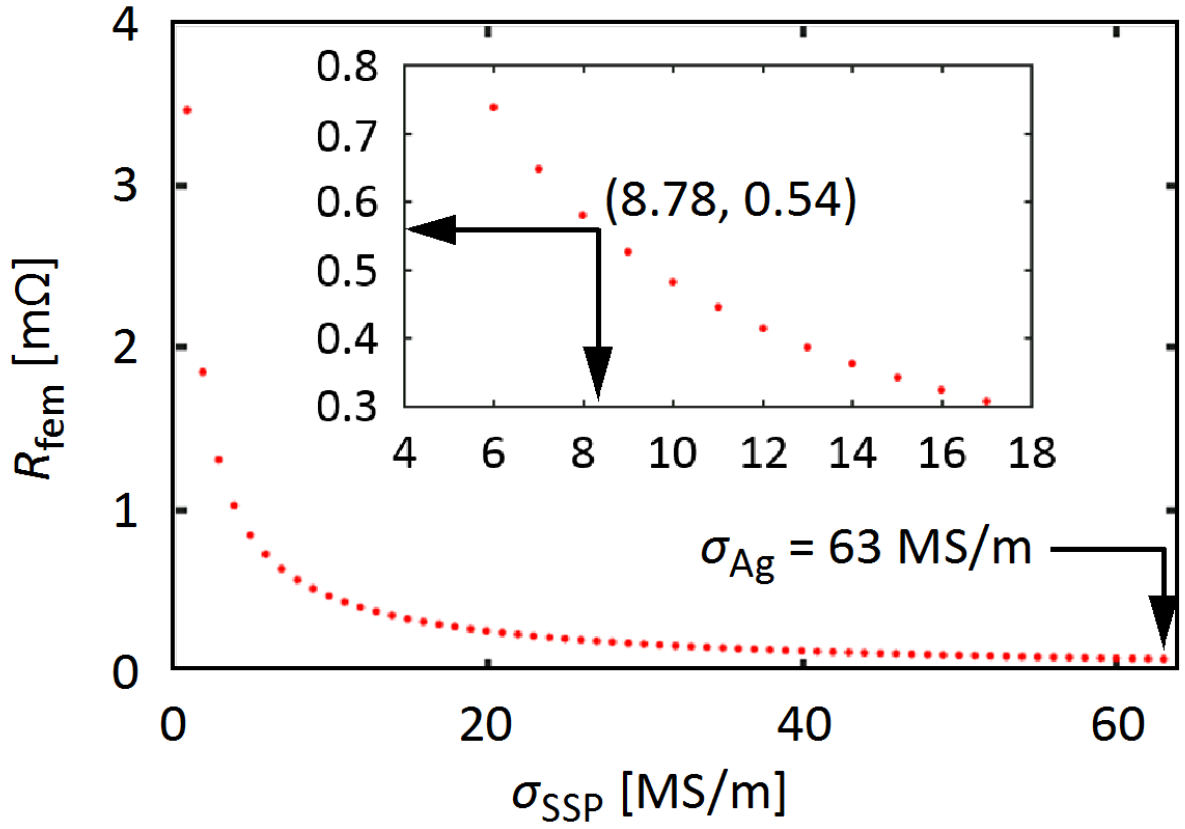

Figure 13. R_{fem} vs. SSP conductivity from FE model.

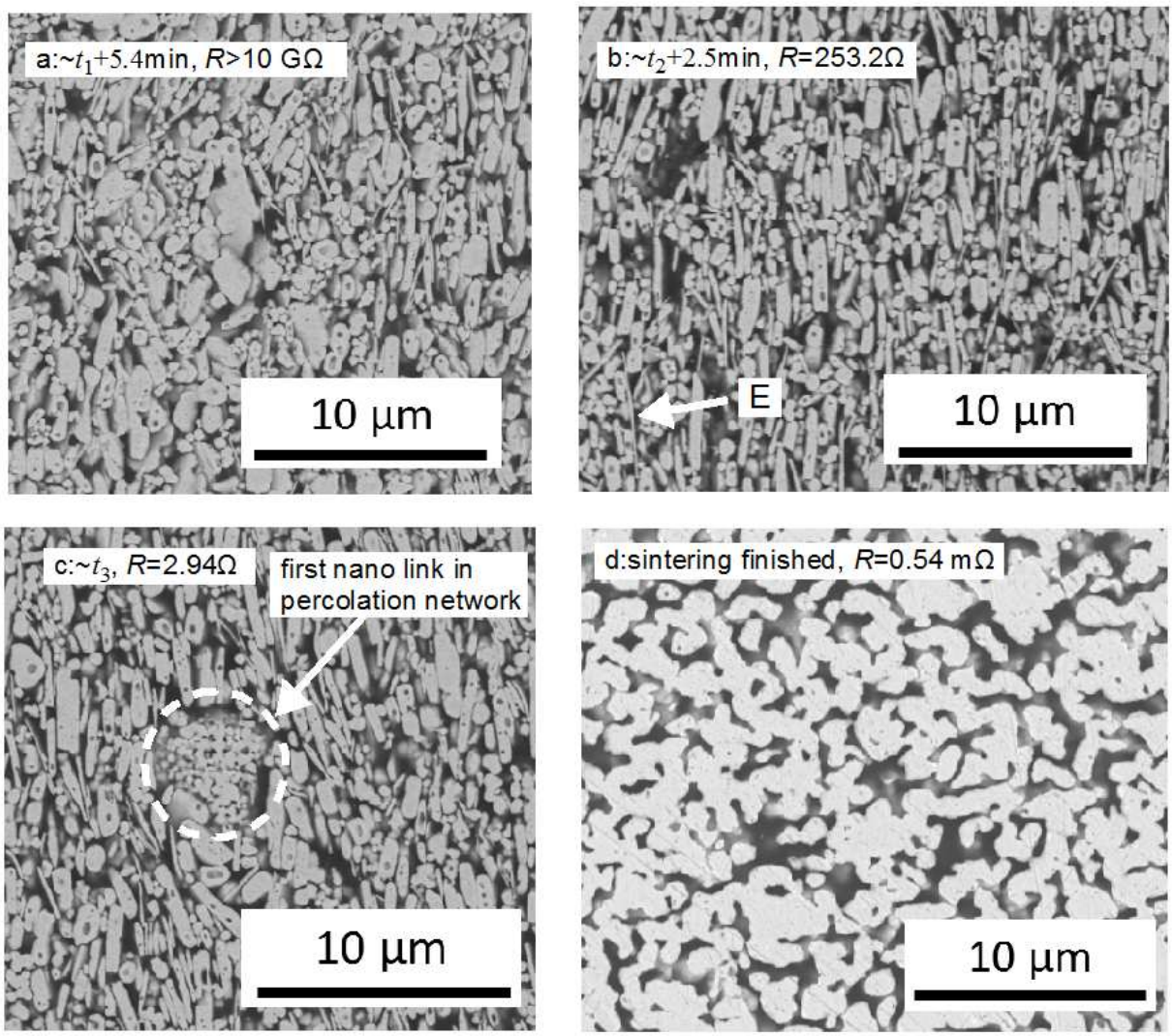

Figure 14. Typical cross-sectional images from samples interrupted (a) between t_1 + 4.7 min and t_1 + 6.1 min, (b) between t_2 and t_2 + 5 min, (c) at about t_3, during the sintering process, and from (d) a sample after sintering is finished. All images are taken with environmental scanning electron microscope (ESEM, Watlab at University of Waterloo).

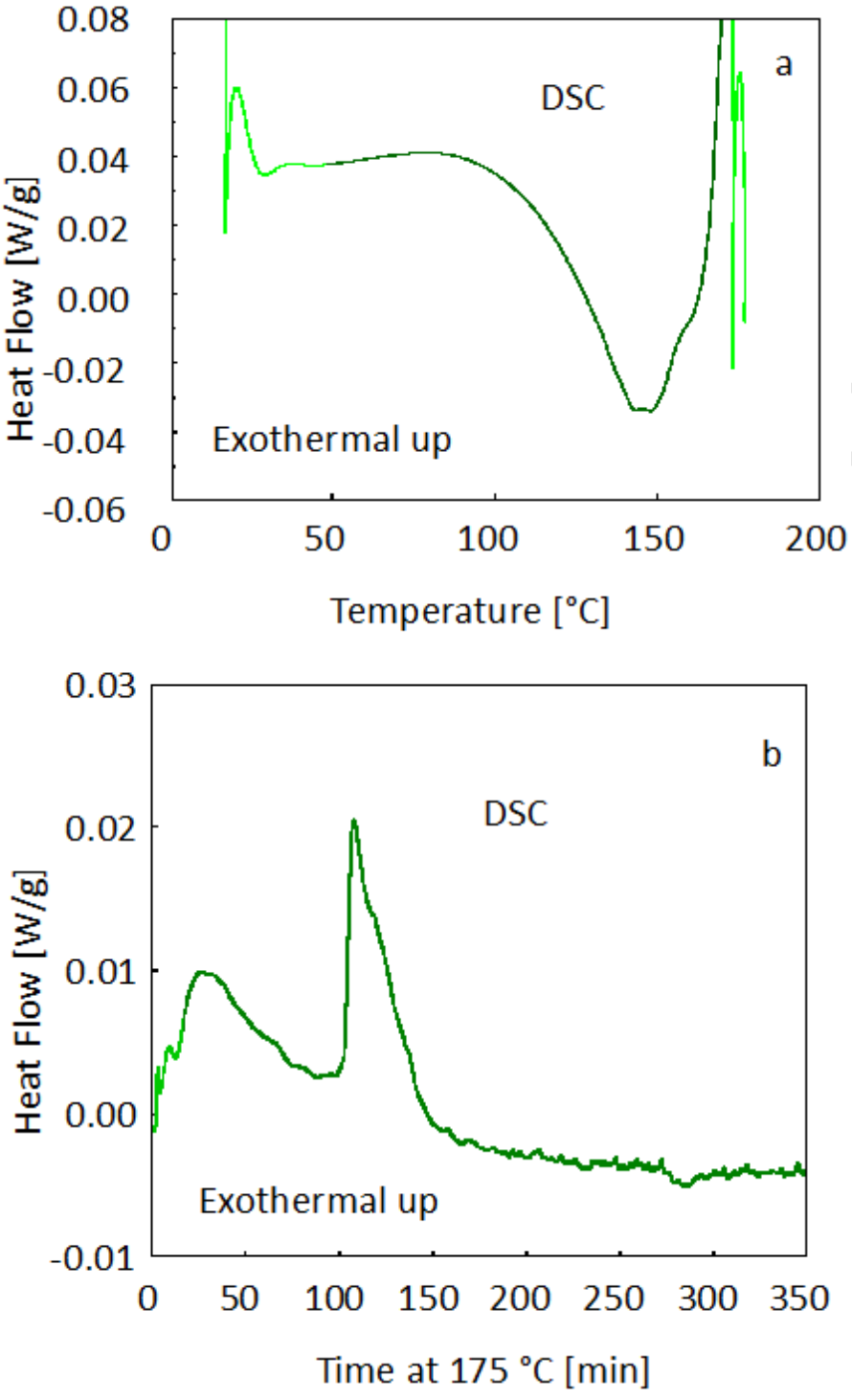

Figure 15. Heat flow vs. (a) temperature during ramping stage from room temperature to 175 °C at a rate of 10 °C/min, and (b) time during subsequent isothermal stage at 175 °C. The noisiness in the light color segments of the curves results from change in temperature..

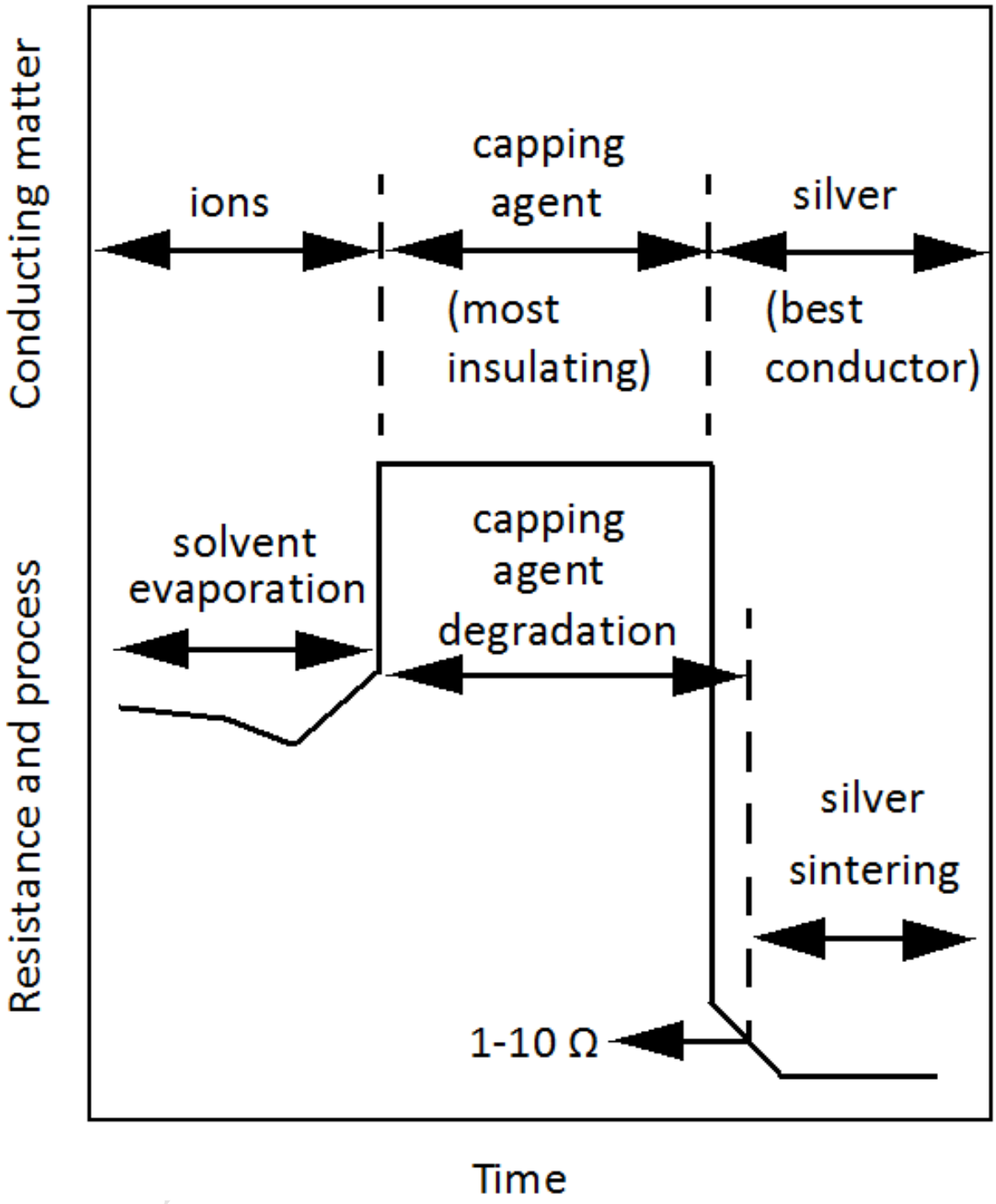

Figure 16. Proposed correlation between resistance signal and the sintering process of the SSP.